Separation and concentration without clogging using a high-throughput tunable filter

E.J. Mossige, A. Jensen, and M.M. Mielnik

Citation:
E. J. Mossige, A. Jensen, and M. M. Mielnik. Separation and concentration without clogging using a high-throughput tunable filter. Phys. Rev. Applied, 2018, vol. 9, issue 5, art. 054007 , pp 11, https://doi.org/10.1103/PhysRevApplied.9.054007

Separation and concentration without clogging using a high-throughput tunable filter

E.J. Mossige[1,3], A. Jensen[1] and M.M. Mielnik[2]

[1]Department of Mathematics, University of Oslo (UiO), Oslo, Norway
[2]Department of Microsystems and Nanotechnology (MiNaLab), SINTEF Digital, Oslo, Norway
[3]Trilobite Microsystems, Kristiansand, Norway

Abstract

We present a detailed experimental study of a hydrodynamic filtration microchip, and show how chip performance can be tuned and clogging avoided by adjusting the flow rates. We demonstrate concentration and separation of microspheres at throughputs as high as 29 mL/min and with 96 % pureness. Results of streakline visualizations show that the thickness of a tunable filtration layer dictates the cut-off size and that two different concentration mechanisms exist. Particles larger than pores are concentrated by low-velocity rolling over the filtration pillars while particles smaller than pores are concentrated by lateral drift across the filtration layer. Results of Particle Image Velocimetry (μPIV) and Particle Tracking Velocimetry (PTV) show that the degree of lateral migration can be quantified by the slip velocity between the particle and surrounding fluid. Finally, by utilizing differences in inertia and separation mode, we demonstrate size-based separation of particles in a mixture.

1 Introduction

Microfluidic separation devices have applications in medical and biological industries, e.g. concentration of microalgae (Chen et al., 2014; Godino et al., 2015) and blood cells (Maria et al., 2015) and in diagnostics (Nam et al., 2016; Warkiani et al., 2015). In the early days of microfluidic separation, cross-flow filtration was a popular separation technique (Lenshof and Laurell, 2010), where the particle cut-off size is given by the filter size. Cross-flow filters are scalable and easy to manufacture but suffer from clogging, which reduces the separation efficiency and reliability. In the search for a clog-free configuration, Yamada and Seki (2005) introduced hydrodynamic filtration in which the flow field was used to control the particle cut-off size instead of the pore size of the filter. Recently, Yamada et al. (2017) improved their initial geometry by using slanted channels. Hydrodynamic filters are cheap, parallelizable and have become commercially available e.g. for blood cell enrichment (Jäggi et al., 2007). However, these filters suffer from low pureness of the processed streams and are restricted to low flow velocities, which limits the throughput.

High throughput can be achieved by utilizing fluid inertia to focus particles to different equilibrium positions based on size (Hood et al., 2016) or shape (Masaeli et al., 2012). The particles are eventually separated by guiding the focused particle sheets through different outlets. In Lim et al. (2014), particles were separated at 50 mL/min in a relatively narrow 80 μm square channel. Despite the high throughput potential, inertial separation devices require high pressures to pump the fluid through long and narrow channels.

The Trilobite microfluidic chip presented in this paper was used previously for the concentration of microalgae (Honsvall et al., 2016) and cancer cells (Dong et al., 2011). Recently, it was demonstrated Mossige et al. (2016) how the flow can be tuned to precisely control the particle cut-off size and concentration ratio. However, only tracer particles were used, and the technology was not demonstrated for separation by using real separation particles.

In this paper, the microfluidic chip is used to separate and concentrate spheres (18, 24, 30 and 69 μm) continuously and at high throughput. By means of streakline visualizations and by measurements of particle concentrations and flow rates, the flow was optimized to maximize concentration ratios and to avoid clogging.

Two different separation mechanisms were identified for spheres; separation by migration along a porous wall, and separation by lateral migration away from this wall. The former was used for separation and concentration of particles larger than the pores with high concentration ratios, while the latter was used to concentrate small particles, even smaller than the pores. Finally, we present flow field velocities by micro Particle Image Velocimetry (μPIV) and particle velocities by Particle Tracking Velocimetry (PTV) to explore the separation and concentration mechanism in detail.

2 Separation principle

The particle separation and concentration is performed by trilobite shaped separation units, see Figure 1. These units consist of a solid wall and a permeable wall with turbine blade shaped pillars which serve to block out and prevent particles from entering the permeate. The distance between these pillars is 25 μm.

An incoming flow of fluid and particles is split in two streams by the separation unit; the permeate stream, which is directed through the permeate outlet, and the concentrate stream, which carries the particles to a concentrate outlet downstream of the separation units. The permeate stream contains few or no particles, and the removal of permeate liquid leads to increased particle concentration in the concentrate stream. With a mixture of particles in the inflow, the permeate stream contains only particles smaller than the distance between pillars.

In Figure 1(a), the fluid velocity is low, and the particles separate from the permeate stream by migration along the permeable wall. The particles interact with this wall without blocking the pores. Low flow velocities lead to a thick flow layer that ends up as permeate, seen as the dotted streamline and denoted as T_p in the figure. The thick flow layer leads to high flux of permeate through the permeate outlet and therefore to high concentration ratios. Separation of smaller particles requires higher fluid velocities, see Figure 1(b). When the fluid velocity increases, the particles separate from the permeate stream by lateral migration away from the permeable wall instead of migration along it. With this separation principle, it is possible to separate

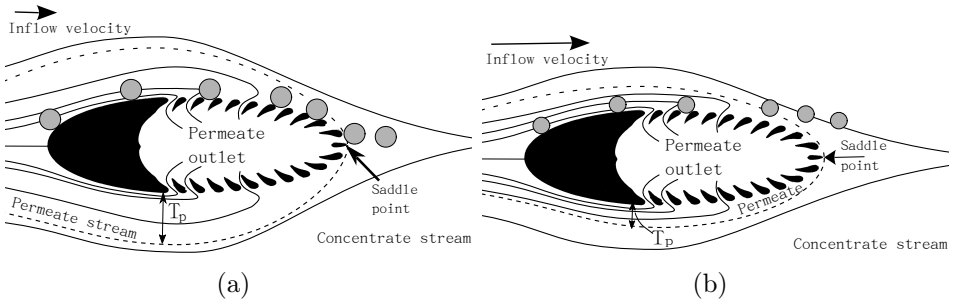

Figure 1: (a) The trilobite shaped separation unit: two different separation principles are shown. In (a), the large particles migrate along the permeable wall and separate without blocking the pores. In (b), the inflow velocity is increased, and the particles separate by lateral migration away from the permeable wall. The flow in (a) is used to separate large particles at high concentration ratios and the flow in (b) is used to separate particles smaller than the gap width between the pillars (25μm).

particles which are smaller than the distance between pillars (25 μm) from the permeate stream. However, the velocity increase from Figure 1(a) to (b) leads to a reduction of T_p and thus to lower concentration ratios. Therefore, large particles in Figure 1(a) can be separated at higher concentration ratios than the small particles in Figure 1 (b).

The combination of the uniform inflow and the permeate outflow leads to a saddle point which in Figure 1 sits directly downstream of the last pillar. However, the saddle point can be moved downstream by increasing the flow of permeate. This increases the concentration ratio but hinders separation because of the strong suction force excerted by the permeate outlet. For particles larger than the pores, this leads to clogging. For particles smaller than pores, this leads to an increase in the particle flux through the permeate outlet and therefore to reduced pureness of the permeate stream.

When the saddle point is moved upstream of the last pillar, the permeate stream is directed back into the main channel, which reduces the concentration ratio. Therefore, the best saddle point position is immediately downstream of the last pillar. This is also discussed in our recent article (Mossige et al., 2016).

3 Experiments

Experimental setup

A schematic of the experimental setup is shown in Figure 2. Central to the setup is a pressure system (MFCS-EZ, Fluigent), which is used to control the throughput Q_{in} and permeate flow rate Q_p by adjusting the pressures in the respective reservoirs. The inlet flow Q_{in} is simply the sum of the two outlet flows, Q_{in}=Q_p+Q_c, where Qc is the flow of concentrate, which is collected in an atmospheric pressure reservoir. A pressure increase in the inflow reservoir leads to an increase in Q_{in}, and a pressure decrease leads to a reduction in Q_{in}. The pressure in the permeate reservoir was primarily adjusted to modify the position of the saddle point. With a pressure increase, the saddle point moved upstream, due to a reduction in Q_p. Likewise, with a pressure decrease the saddle point moved downstream, due to an increase in Q_p. The concentrate flow rate Q_c and the permeate flow rate were measured using laboratory scales (Mettler Toledo, ML303T) and continuously monitored to check for potential fluctuations. The flow rates were easily reproduced because the flow rates are linear functions of the reservoir pressures.

To get rid of gas cavities and bubbles, the flow system was flushed prior to each experiment, by applying a high inlet pressure. A low permeate reservoir pressure was applied to create a high suction force through the permeate outlet.

The flow fields and particle separation regimes were characterized by streakline visualizations and by fluid and particle velocimetry (μPIV and PTV, respectively). Fluorescent tracer particles (Life Technologies, 1 μm,CA, USA) that accurately follow the flow were used to visualize the flow fields, particularly around the saddle point, and for flow velocity measurements. Fluorescent polymer spheres (Cospheric LLC, CA, USA) with mean diameter of 21, 24, 32 and 69 μm were used as separation particles and for velocity measurements by Particle Tracking Velocimetry (PTV). These are listed in Table 1. A continuous light source (Olympus U-HGLGPS) was used in combination with a filter set for green light excitation (ZET532/10x, Chroma) to illuminate these fluorescent particles. Objectives with magnification 10x (Olympus PlanC N 10x/0.25) and 20x (Olympus UPlanFL N 20x/0.50) were used for the visualizations and images were captured with a CCD camera

(pco, pco.4000) which was mounted onto the upright microscope (BX43, Olympus). For the flow and particle velocity measurements, a double pulsed Nd:YAG laser (Litron nanoPIV) was used as light source (wavelength 532nm, i.e. green light) and the time difference between the two successive laser pulses was controlled with a LabView program, typically 6 μs. The 20x-objective was used for all the velocity measurements and the particle image pairs were processed with an in-house made ensemble average PIV algorithm to extract the flow velocity fields. A thresholding technique was applied to extract the particle velocities from the same images, which were captured at the centerplane, halfway between the channel bed and the glass lid. Due to the low particle concentrations, about 1 particle per 3 exposures, the images were stacked on top of each other to synthetically increase the number of particles in each image used for the PTV-calculations.

The particle concentrations were determined by counting the number of particles in 2 μL drops, dispersed onto a microscope slide and viewed through a 4x-objective (Olympus PlanC N 4x/0.10).

Microfluidic chips

The microfluidic chips, see Figure 2 and 3, were manufactured by SINTEF MiNaLab using standard micromachining processes. The process is described in Mossige et al. (2016). In the chip layout presented in this paper, an array of 13 trilobite units, 460 μm wide and 1155 μm long, makes up the separation section in the 90 μm deep main channel. With 740 μm from center to center, these units block 62 % of the channel cross sectional area. Branching channels connect the inlet and concentrate outlet to the main channel, which is 10 mm wide and 30 mm long.

The high pressure drop resulting from abrupt changes in the fluid volume can cause the liquid to degas. This, in turn, can lead to bubble formation. To reduce the pressure drop in the entrance region to the main channel, quadratic cylinders were placed upstream and downstream to effectively remove this problem.

A 300 μm thick glass slide was bonded onto the fluidic chip for sealing and viewing purposes. The chips were cleaned between each experimental run by using a syringe to flush the channels with acetone, propanol and deionized

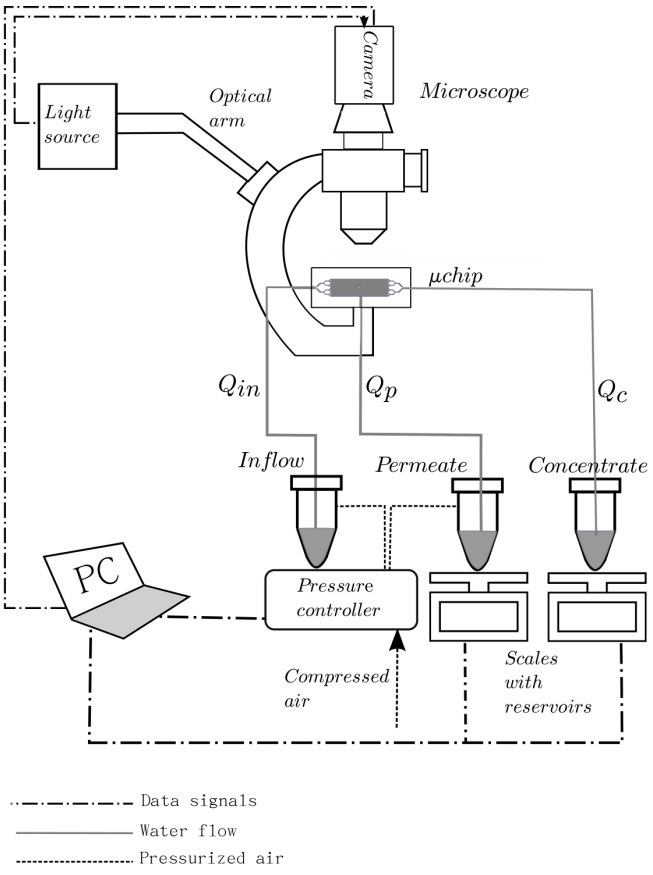

(a)

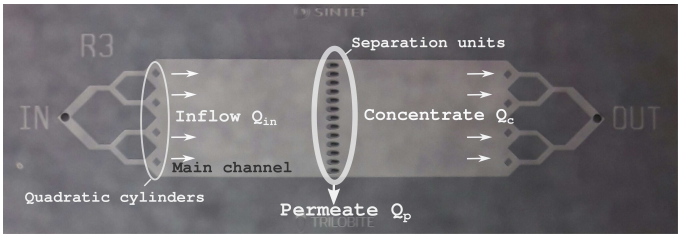

(b)

Figure 2: (a) Experimental setup. A pressure system and laboratory scales are used to control the flow rates Q_{in}, Q_p and Q_c. The particles are illuminated with continuous light for the streakline visualizations, and with a pulsed Nd:YAG laser for the μPIV and PTV measurements. (b) Microfluidic chip. The main channel is 30mm long, 10mm wide and 90 µm deep with 13 separation units.

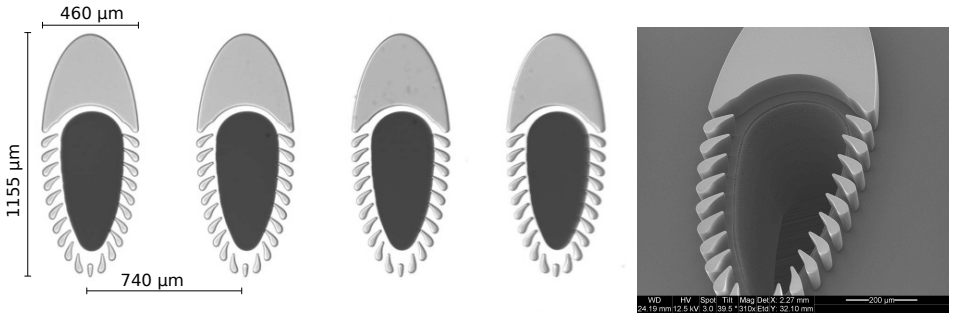

(a) (b)

Figure 3: (a) A close-up of four separation units, rotated 90 °. Each unit is 460 μm wide and 1155 μm long, and the distance from center to center is 740 μm. (b) SEM image of one single separation unit.

water. In addition, piranha solution, which is a mixture of sulfuric acid and hydrogen peroxide, was injected into the channels. A glass syringe was used for the injection since the strong piranha solution does not dissolve glass. For details on the piranha preparation procedure, see e.g. Kern (2007).

The inlet and outlets on the chip were connected to the reservoirs by tubing and an in-house made chip holder machined in acrylic glass. The inlet and concentrate outlet on the chip holder were circular (1 mm diameter), while the permeate outlet, shared by all the trilobite separation units, was a rectangular channel (1 by 10 mm).

Particles

The microspheres used to study separation and for velocity measurements by PTV are called "separation particles" and are referred to as D_{p18}, D_{p24}, D_{p30} and D_{p69} in the text, respectively. D_{p18} and D_{p24} are referred to as small particles, and D_{p30} and D_{p69} are referred to as large particles. These neutrally buoyant particles (1±0.01 g/cc) were dispersed in deionized water at 25 °C. An overview of the different particles used in this study is shown in Table 1.

Tracer particles (1 µm mean diameter), used for µPIV and for fluid flow visualizations, were mixed with the separation particle solutions to a concen-

tration ratio of $1.14 \cdot 10^{-5}$ by volume. Surfactant Triton-X (Sigma Aldrich) was added to the particle solutions to prevent bubble formation and particle agglomeration to the walls and coverslip surface.

	Separation particles				Tracers
Group	Small		Large		-
Diameter (D_p)	18μm	24μm	30μm	69μm	1μm
Reference name	D_{p18}	D_{p24}	D_{p30}	D_{p69}	-
Concentration[v/v]	$1.71 \cdot 10^{-5}$	$8.57 \cdot 10^{-5}$	$8.57 \cdot 10^{-5}$	$6.86 \cdot 10^{-5}$	$1.14 \cdot 10^{-5}$
Density [g cc^{-1}]	1.0	1.0	1.0	1.0	1.05
Excitation [nm]	300-600	300-600	300-600	300-600	450-580

Table 1: Separation particles and tracer particles used in the experiments.

4 Results

4.1 Separation Phenomena and Performance

Calibration of the system without particles

In order to determine the flow rates, Q_{in} and Q_p, which gave the desired position of the saddle point and extent of flow layer T_p, the system was calibrated by streakline visualizations using tracers. Our results showed that an increase in the throughput Q_{in} led to an increase of permeate, Q_p, when the pressure in the permeate reservoir was kept constant. As a consequence of the increased suction, the saddle point moved downstream. Likewise, a decrease in Q_{in} led to a reduction of permeate, which was followed by an upstream displacement of the saddle point. Figure 4 shows streakline visualizations of an upstream (a) and downstream (b) saddle point.

To keep the saddle point fixed when Q_{in} changed, Q_p had to be altered by adjusting the pressure in the permeate reservoir. The saddle point was moved upstream by increasing the pressure in the permeate reservoir (which reduced the permeate flux) and moved downstream by decreasing the pressure in the permeate reservoir (which increased the permeate flux).

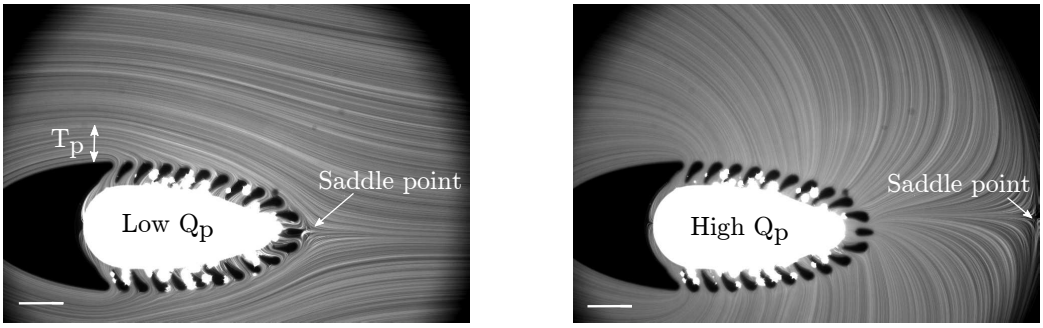

(a) (b)

Figure 4: Streaklines obtained using tracer particles using a single trilobite unit show (a) an upstream saddle point resulting from low suction Q_p and (b) a downstream saddle point resulting from high suction Q_p. The flow field in (a) was generated by applying a high permeate reservoir pressure while the flow field in (b) was generated by applying a low permeate pressure. In (a), T_p is small which enables separation while in (b) T_p is larger (extends outside the field-of-view of the image) which hinders separation. The white dots are agglomeration of dust and tracer particles, but these do not influence the flow. Scale bar is 100 μm.

The flow layer T_p also varied with Q_{in}. When the saddle point was fixed near the last pillar, an increase in the inflow led to a reduction of T_p. In our recent article (Mossige et al., 2016), where tracers but no separation particles were used, it was hypothesized that the layer thickness can be used to manipulate the particle cut-off size. It was postulated that the particle center-of-mass must be outside the permeate layer for successful separation; it would then be carried by the concentrate flow, away from the filtration pillars. To ensure this, the particle must be at least twice the size of the filtration layer. For spheres this yields $D_p > 2T_p$.

Our measurements show that the pressure driven flow fields were stabilized by increasing the flow rates. This is because a pressure increase in the reservoirs led to a dampening of the pressure fluctuations. For the flow field used for separation, the magnitude of the fluctuations were less that 1 %, scaled by the mean pressures in the reservoirs. Correspondingly, the fluctuations in flow rates were also 1 %, measured by laboratory scales. By applying the maximum pressure (7 bar) available with our system, the highest throughput achievable was 32 mL/min.

After calibration, the flow fields were easily reproduced by imposing pre-calibrated pressures, with only 1 % variation between experiments.

The permeate outlets on the Trilobite separation units were connected to each other via a shared outlet channel for the permeate fluid. The pressure drop required to push the fluid through this channel and into the tubing (that connected the fluidic chip to the permeate reservoir) led to a slight variation in the pressures at the different permeate outlets. Naturally, this led to variation in the saddle point positions across the array of separation units. To avoid clogging, the flow was adjusted such that the saddle points were never downstream of the last pillar for any of the separation units.

Separation regimes and influence of saddle point position

The streakline visualizations in Figure 5 illustrate the two different separation mechanisms we observed for the Trilobite filter, namely wall- and lateral migration. The separation particles create the thick streaks, and the tracers create the thin streaks, used to visualize the fluid flow. In Figure 5(a-b), the particles are larger than the pores and separate from the permeate flow by wall migration at low fluid velocities. In Figure 5(c-d), the particles are smaller than the pores and separate by lateral migration, at high fluid velocities.

The streakline visualizations in Figure 6 show how the saddle point position dictates the separation performance. In (a), the saddle point is immediately downstream of the last pillar which leads to successful separation of 18 μm particles. However, when the saddle point is moved downstream (Figure 6 (b)), these particles cannot separate from the permeate, due to the high permeate suction. As a result, the particles follow the streamlines into the permeate outlet. In Figure 6(c), the saddle point is still downstream of the last pillar, however now the particles are larger than the pores. This immediately leads to clogging which, in turn, pushes the saddle point even farther downstream. The repositioning modifies the flow field directs the flow inwards towards the pillars. This further suppresses separation and amplifies the clogging, as seen in Figure 6(d).

The presence of separation particles does not affect the flow rates when clogging does not occur. Particularly, the injection of particles did not influ-

ence the position of the saddle point, as seen in Figure 6(a) and (b). When clogging occurred however (Figure 6(c) and (d)), the flow rates were reduced. By monitoring the flow rates it was therefore possible to detect clogging without the need for visual inspection.

Concentration and filtration performance

The concentration ratio φ_c is the ratio of particle concentrations in the concentrate, C_c, to the particle concentration in the inflow, C_{in}. Maximization of the concentrate ratio is achieved through maximizing the permeate flux ratio, defined as Q_p^*=Q_p/Q_{in}. In the experiments, this was done by finding the minimum inflow Q_{in} required to separate each type of particle (18, 24, 30 and 69 μm). The permeate flux was adjusted to fix the saddle point near the last pillar.

Table 2 is a list of the minimum flow rates required for separation, Q_{in}, the permeate flux, Q_p, and the maximum permeate flux ratio, Q_p^*. Attempting to increase Q_p^* above these maximum values leads to clogging because it can only be achieved by moving the saddle point downstream of the last pillar. Our results show that Q_p^* increases with particle size. This is because the separation of large particles can be performed at low flow rates Q_{in}, and because the low throughput did not lead to a reduction in Q_p. The reason why large particles can be separated at low velocities is that lateral migration is not necessary. For instance, 10 mL/min was sufficient to separate D_{p69}, while a threefold increase to 32 mL/min was required to induce the lateral migration required to separate D_{p18} and D_{p24}.

Along with the flow rates, measures of concentration and filtration performance are presented in Table 2. The filtration ratio φ_p is a measure of the pureness of the permeate stream and is defined as $\varphi_p = 1 - \frac{C_p}{C_{in}}$, where C_p is the particle concentration in the permeate and C_{in} is the particle concentration in the inflow. For D_{p18}, the filtration ratio φ_p is 0.43, and for D_{p24}, the filtration ratio is as high as 0.96, i.e. the permeate particle concentration is only 4% of the inflow particle concentration. Since D_{p30} and D_{p69} are larger than the gaps between the pillars (25 μm) they cannot enter the permeate, hence φ_p=1.

High pureness is important in purification processes such as the removal

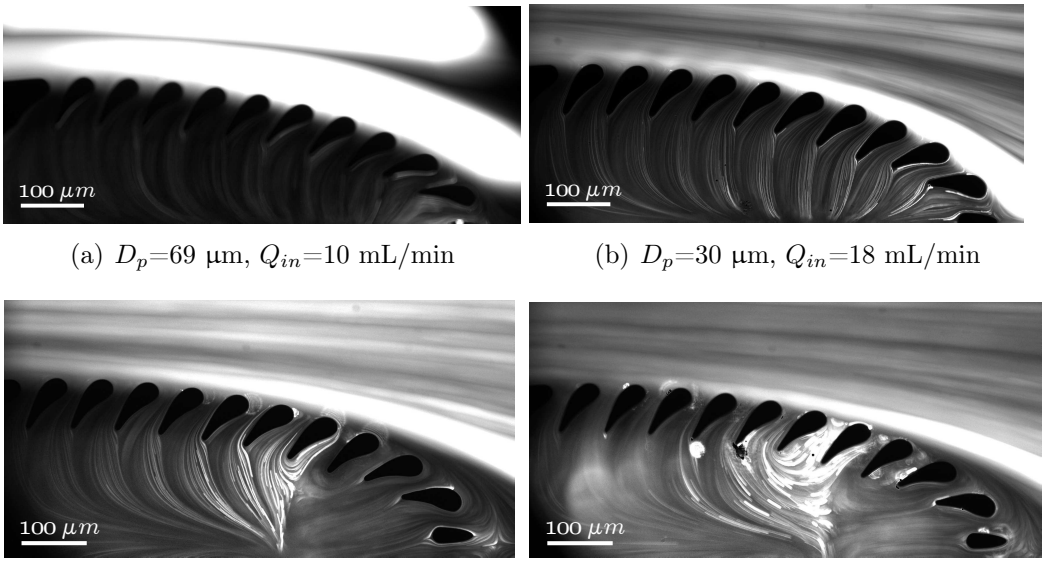

(a) D_p=69 µm, Q_{in}=10 mL/min

(b) D_p=30 µm, Q_{in}=18 mL/min

(c) D_p=24 µm, Q_{in}=32 mL/min

(d) D_p=18 µm, Q_{in}=32 mL/min

Figure 5: Streaklines that show the different separation mechanisms. The separation particles create the thick streaks, and the tracers create the thin streaks, used to visualize the fluid flow. The large particles, 69 µm in (a) and 30 µm in (b), separate from the permeate flow by migration along the wall at low fluid velocities. The movie "separationDp30.mov" in the electronic supplementary information (ESI) shows separation of the 30 µm particles in (b). The small particles, 24 µm in (c) and 18 µm in (d), separate from the permeate flow by migration across the streamlines of the flow at high fluid velocities. The saddle point is located directly downstream of the last pillar.

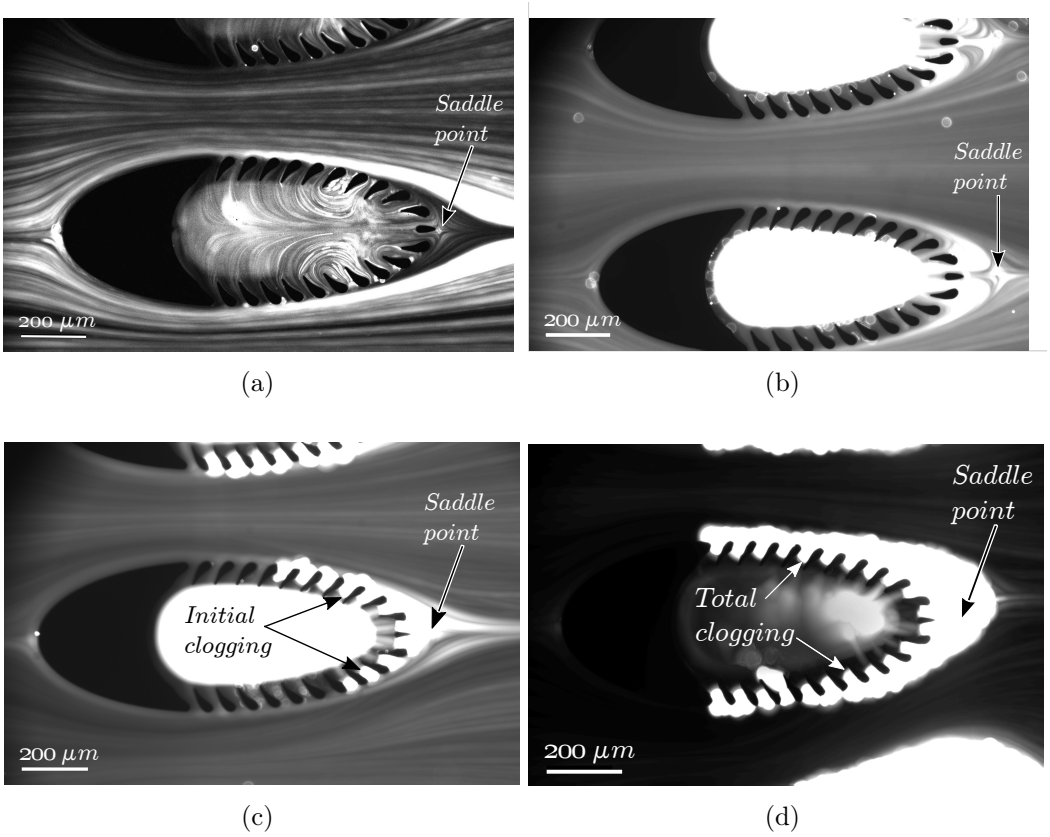

Figure 6: Streakline visualizations that show the importance of a correct saddle point position. The flow in (a) has saddle point near the last pillar, seen as converging streaklines produced by the tracer particles. The particles (18μm) separate successfully from the permeate flow because the saddle point is sufficiently far upstream. In (b), the saddle point is moved downstream and the particles no longer separate from the flow. Instead, they end up in the permeate outlet. In (c) and (d), the particles are larger than the pore size and clog the permeable wall because the saddle point is too far downstream.

Flow rates				Performance	
D_p	Q_{in}	Q_p	Q_p^*	φ_c	φ_p
$D_{p18}(18\mu\text{m})$	32.0	2.6	0.08	1.04	0.43
$D_{p24}(24\mu\text{m})$	32.0	2.6	0.08	1.08	0.96
$D_{p30}(30\mu\text{m})$	18.8	2.9	0.15	1.18	1.00
$D_{p69}(69\mu\text{m})$	10.1	3.0	0.29	1.42	1.00
Unit	$\frac{\text{ml}}{\text{min}}$	$\frac{\text{ml}}{\text{min}}$	-	-	-

Table 2: Flow rates and performance parameters for particles with diameters D_p. Q_{in} is the minimum influx and Q_p is the maximum permeate flux that ensure separation. The ratio Q_p/Q_{in} the permeate flux ratio Q_p^*. φ_p is the filtration ratio and φ_c is the concentration ratio.

of contaminants to produce drinking water. In these types of processes, only a very low concentration of particles can be accepted in the stream used for drinking water as contaminants could be harmful and lead to disease. In other words, φ_p in the permeate stream must be lower than some threshold. By looping the permeate stream, higher pureness is possible for particles smaller than the gap width.

For D_{p18}, the increase in particle concentration is 4% from inlet to concentrate outlet, while for D_{p69}, the increase is as much as 42%. The reason why the separator performs better for the large particles is that the permeate flux ratio Q_p^* increases with size, and that all the particles are concentrated, i.e., φ_p=1.

High concentration ratios are crucial in many industrial and medical applications. In industrial bioengineering processes, such as in microalgae harvesting, a high concentration of algae is required to get a usable product. In medical applications, such as the study of live cells under the microscope, a dense population of cells is important in order to obtain statistically significant results. For our device, the concentration ratio can be increased by looping the concentrate flow or by adding separation units downstream or upstream of the existing row of separation units. The same can be achieved with a series arrangement of microfluidic chips.

Figure 7 shows separation and clogging regimes for particles with diameters D_p (x-axis). The minimum inflow Q_{in} that ensures separation is plotted in

Figure 7(a), and the maximum permeate flux ratio Q_p^*, is plotted in Figure 7(b). "High φ_p" means at least 43% pureness, i.e. $\varphi_p > 43\%$, which is the pureness for D_{p18}, and "low φ_p" means $\varphi_p < 43\%$. The plots show that large particles could be separated at lower flow rates Q_{in} and higher permeate flux ratios Q_p^* than small particles, and that both D_{p18} and D_{p24} are separated with high pureness φ_p, i.e. $\varphi_p > 43\%$. The error bars indicate the massflow variation, which was 1%.

4.2 Flow Field and Particle Velocities

Flow field velocities

Figure 8 shows a vector plot of the velocity fields used to concentrate the spheres larger than the pores, D_{p69} (a) and D_{p30} (c). The circles indicate the particle size and the solid line is the thickness of the permeate flow layer. Figure 8(b) and (d) show flow details around the particles. The velocity increase from Figure 8(a) to (c) leads to a thinning of the permeate layer due to the decrease in permeate flux.

In our previous article (Mossige et al., 2016) it was hypothesized that the particle center-of-mass must be outside the permeate layer for successful separation. This yields $D_p > 2T_p$ as minimum cut-off. This hypothesis was based on results of streakline visualizations and PIV velocimetry using tracers. However, our measurements using separation particles show that $D_p > 2T_p$ is too strict and that separation is possible for particles comparable in size to the separation layer, i.e. $D_p > T_p$. This is shown in Figure 8, where T_p is 60 µm for 69 µm spheres (a), and 32 µm for 30 µm spheres (b). This new knowledge means that smaller particles can be separated than postulated in (Mossige et al., 2016) and that higher concentration ratios can be achieved.

Figure 8(b) and (d) show that the particle size is comparable to the thickness of a shear layer which, in turn, is comparable to the permeate thickness. Particles inside this layer experience a strong velocity gradient, which induces rotation. The resulting rolling over the porous wall prevents clogging.

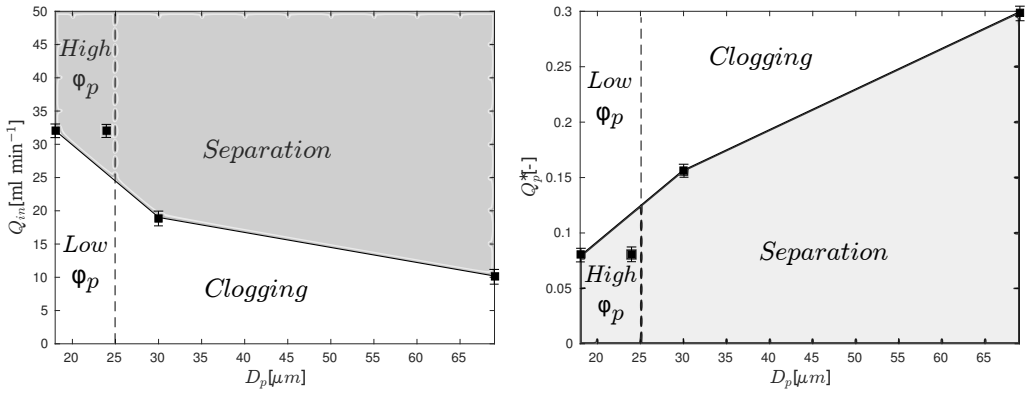

(a) (b)

Figure 7: Separation and clogging regimes for particles with diameters D_p (x axis) with minimum inflow Q_{in} (a) and maximum permeate flux ratio Q_p^* in (b). The plots show that large particles (>25 μm) can be separated at lower flow rates Q_{in} (a) and higher permeate flux ratios Q_p^* (b) than small particles (<25 μm). The dotted line indicates the pore size (25 μm). "High φ_p" means at least 43% pureness, i.e. $\varphi_p > 43\%$. This is the pureness obtained for D_{p18} with the highest flow rate available with the setup (32 mL/min). "low φ_p" means $\varphi_p < 43\%$, which is the case if the flow rate is reduced below 32 mL/min or the saddle point is moved downstream. The massflow fluctuations from the mean of each experiment as well as the variation of the mean massflow between experiments was 1%, shown by the error bars.

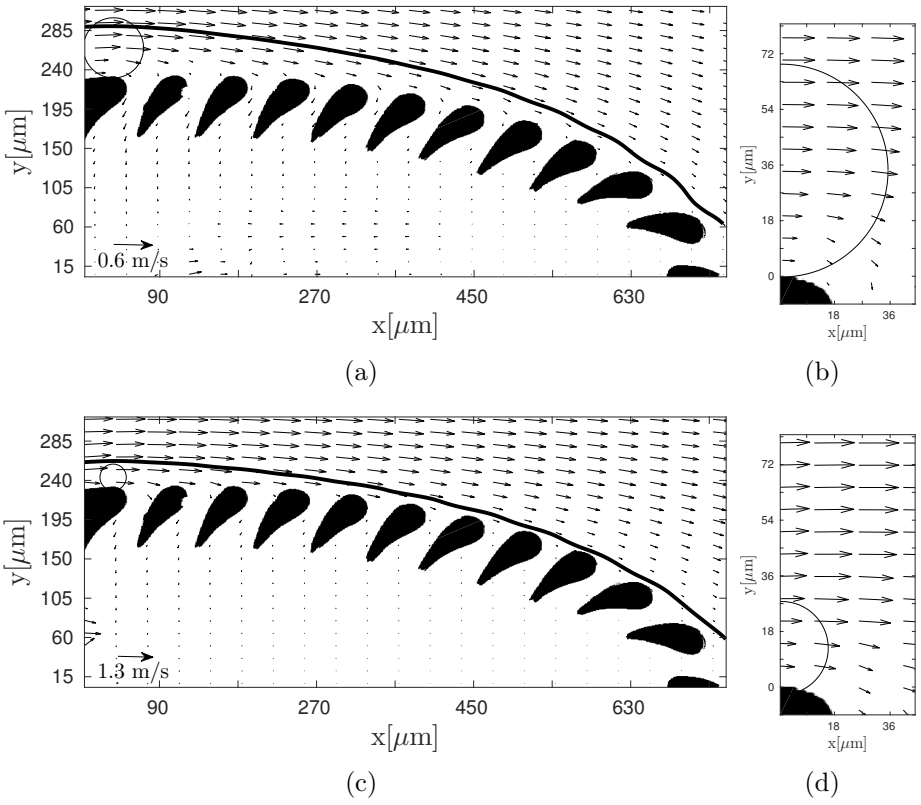

Figure 8: Vector plots of velocity fields used to separate D_{p69} (a,b) and D_{p30} (c,d), where (b) and (d) are zoom views around the particles. The circles indicate the typical particle size and the solid line is the permeate streamline. The particles are comparable in size to the permeate layer thickness in (a) and (c), which is the cut-off size; $D_p > T_p$. The particles are also comparable in size to the shear layer thickness in (b) and (d).

Particle velocities

Figure 9 shows the particle (red vectors) and fluid flow velocities (black vectors) taken in the particle center-of-mass, under flow conditions given in Table 2. In Figure 9(a-b), the particles (D_{p69} and D_{p30}, respectively) are larger than the pores and migrate along the pillars at low velocities. In (a), the three left-most particles (D_{p69}) are inside the permeate layer. The particle velocities can be easily distinguished from the fluid velocities and are directed more inwards, towards the filtration pillars. This is an indication of rolling over the wall due to the shear within the permeate layer. The two right-most particles are outside this layer, which shrinks with downstream distance along the pores. Since they get associated with streamlines in the concentrate flow, their velocities are directed away from the permeable wall. Thus, since the particles are much larger than the thin permeate layer in the downstream region, they experience some degree of lateral displacement. However, this is a size effect and is not due to inertia. Figure 9(b) shows velocities of D_{p30}. Compared to the situation in (a), the particles in the downstream region are much closer to the pillars. This is because the centers of these particles are inside the permeate layer. Thus, their velocitities are also much more similar to the corresponding fluid velocities than in (a) as these particles experience no lateral migration under the current flow conditions.

In Figure 9 (c-d), the particles (D_{p24} and D_{p18}, respectively) are smaller than the pores. Compared to the rolling regimes in Figure 9 (a-b), fewer particles were observed in the region directly downstream the filtration structures. This is due to migration across streamlines. Because this migration is induced by inertia, it is particularly effective in regions of high streamline curvature, such as near the saddle point. The effect is also more pronounced for larger particles, as evidenced by fewer particles in vicinity of the filtration structure in the downstream region for D_{p24} as compared to D_{p18}. This also explains the difference in separation efficiency between the two particle sizes; 96% vs. 43% pureness.

Finally, Figure 9 (e-f) are zoom views of the regions inside the dashed rectangles in Figure 9 (c-d). These figures show clearly that the particle velocities are directed outwards compared to the corresponding fluid velocities. Again, this shows particle migration across the streamlines.

Theoretically, this can be rationalized by considering the slip Reynolds number, which is a measure of the amount of inertia in the fluid surrounding the particles. The drag force causes the particles to lag behind the fluid (Maxey and Riley, 1983), giving rise to the slip velocity $U_s = u_p$ - U_p, where u_p is the fluid velocity taken in the geometrical center of the particles and U_p is the corresponding fluid velocity. The slip Reynolds number is defined as $Re = U_s\, D_p\, \nu^{-1}$, where ν is the kinematic viscosity of the fluid. The slip velocity for D_{p18} and D_{p24} was measured to be 0.4 and 0.5 m/s, which yields Re of 7 and 13, respectively, indicating stronger inertial migration for D_{p24}, in agreement with our experimental observation. Note that the Re cannot be used to differentiate between lateral- and wall migration, since the latter is a size effect where the movement of particles is dictated by the combination of the flow-induced hydrodynamic forces and the physical obstruction caused by the filtration pillars.

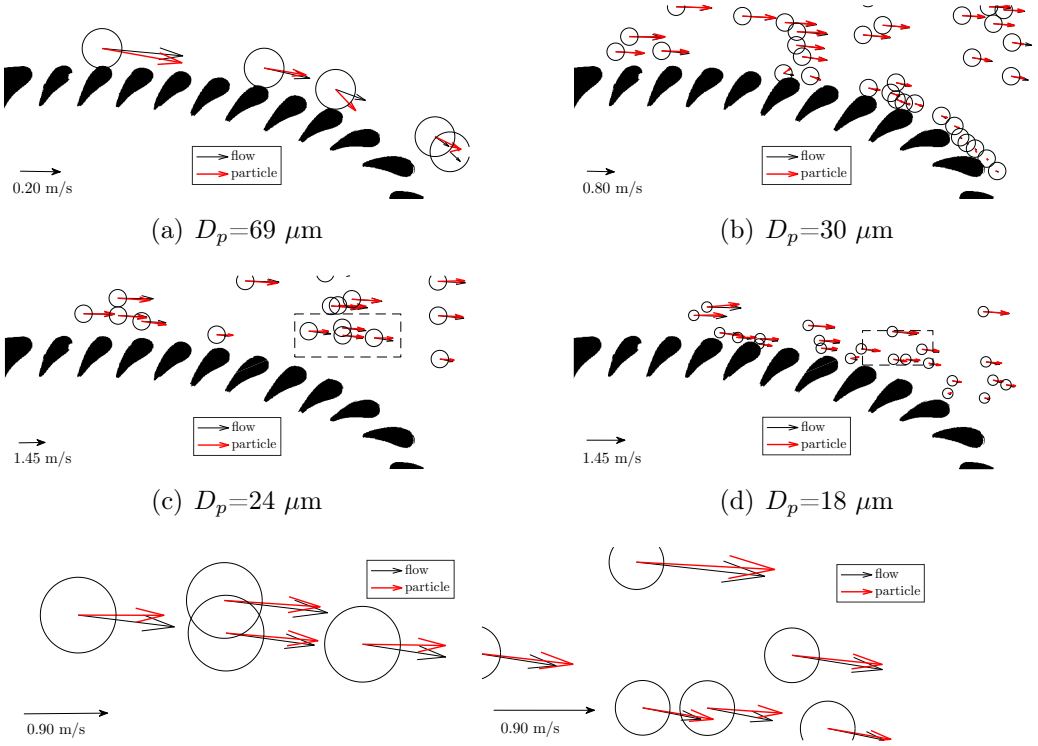

(a) D_p=69 μm (b) D_p=30 μm

(c) D_p=24 μm (d) D_p=18 μm

(e) D_p=24 μm (f) D_p=18 μm

Figure 9: Particle vectors (red) and flow velocity vectors in the center of the particle (black). The large particles in (a) and (b) separate at low velocities by migration along the wall, wheres the small particles in (c) and (d) separate at high velocities by migration across streamlines. The zoom view in (e) and (f) show that the particle velocity vectors in (c) and (d) are directed more outwards, away from the wall, than the corresponding fluid velocities.

5 Separation of particles by size

Our results with individual particles indicate that size-based separation in a mixture is possible. In order to verify this, we performed separation of particles larger than pores from particles smaller than pores. Figure 10 is a streakline visualization of size-based separation of 30 and 69 μm spheres from 18 μm spheres. Due to the dewatering through the permeate outlet, the large particles are simultaneously concentrated. With the employed flow rate, 18 mL/min, the flow velocity was sufficiently high to induce rolling over the pillars and to avoid clogging for D_{p30}. However, the flow rate was too low to induce lateral drift away from the pillars for D_{p18}. Therefore, these particles followed the flow of permeate through the filtration pores and were thus successfully separated from the large spheres.

The flow velocity was sufficiently high to induce lateral drift for 69 μm spheres. The migration across streamlines was enhanced by the fact that these particles are larger than the permeate flow layer, i.e. $D_p > T_p$, and therefore get associated with streamlines in the concentrate flow region. As a result, there are no 69 μm particles directly downstream of the separation unit (only 18 and 30 μm). The difference in lateral displacement between 30 and 69 μm spheres can be utilized as a new separation method, for particles larger than pores. By directing the particles through separate outlets downstream of the separation units, efficient fractionation by size is possible.

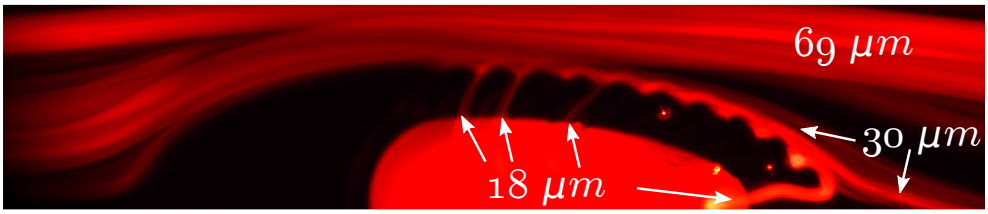

Figure 10: Simultaneous concentration and separation of 18 μm from 30 and 69 μm spheres, shown by streaklines. The flow rate Q_{in} is 18 mL/min which is the velocity required to separate 30 μm spheres by migration along the pillars. The 18 μm spheres follow the flow of permeate through the pillar gaps because the velocity is too low to induce lateral drift away from the pillars. However, the velocity is sufficiently high to induce lateral migration of the largest (69 μm) spheres. Due to the high degree of lateral displacement, these can be separated from the 30 μm spheres downstream of the separation units.

6 Conclusion

Filtration and concentration of rigid spheres without clogging was performed with throughputs as high as 29 mL/min and with 96 % pureness. Two different filtration mechanisms were identified, namely concentration by particle migration along the permeable wall, and concentration by lateral drift across streamlines. The former was used to concentrate particles larger than pores at low slip velocities and with high concentration ratios, while the latter was used to concentrate particles smaller than pores by utilizing inertia. It was found that the cut-off size was given by the permeate layer thickness, which is an improvement compared to earlier predictions.

The filter performance was found to rely heavily on the saddle point position. The optimal position of the saddle point was found to be immediately rear of the filtration unit. With this position, the clog-free property was conserved while the concentration ratio was maximized. Moving the saddle point upstream of this position reduced the concentration ratio, while moving it downstream led to clogging.

By utilizing the difference in inertia and separation mode, we showed that the filter can be utilized for efficient size-based separation. This is achieved through a combination of direct filtrate-retentate separation and by size-based lateral positioning downstream of the filtration unit.

Acknowledgments

This project was funded by Trilobite Microsystems A/S and The Research Council of Norway - project number 232148. Support was also received from the Norwegian micro- and nanofabrication Facility (NORFAB) infrastructure project.

References

Chen, C.-C., Chen, Y.-A., Liu, Y.-J., and Yao, D.-J. (2014). A multilayer concentric filter device to diminish clogging for separation of particles and

microalgae based on size. *Lab Chip*, 14:1459–1468.

Dong, T., Yang, Z., Su, Q., Tran, N. M., Egeland, E. B., Karlsen, F., Zhang, Y., Kapiris, M. J., and Jakobsen, H. (2011). Integratable non-clogging microconcentrator based on counter-flow principle for continuous enrichment of caski cells sample. *Microfluidics and Nanofluidics*, 10(4):855–865.

Godino, N., Jorde, F., Lawlor, D., Jaeger, M., and Duschl, C. (2015). Purification of microalgae from bacterial contamination using a disposable inertia-based microfluidic device. *Journal of Micromechanics and Microengineering*, 25(8):084002.

Honsvall, B. K., Altin, D., and Robertson, L. J. (2016). Continuous harvesting of microalgae by new microfluidic technology for particle separation. *Bioresource Technology*, 200:360 – 365.

Hood, K., Kahkeshani, S., Di Carlo, D., and Roper, M. (2016). Direct measurement of particle inertial migration in rectangular microchannels. *Lab Chip*, 16:2840–2850.

Jäggi, R. D., Sandoz, R., and Effenhauser, C. S. (2007). Microfluidic depletion of red blood cells from whole blood in high-aspect-ratio microchannels. *Microfluidics and Nanofluidics*, 3(1):47–53.

Kern, W. (2007). RCA Critical Cleaning Process. Technical report, RCA clean.

Lenshof, A. and Laurell, T. (2010). Continuous separation of cells and particles in microfluidic systems. *Chem. Soc. Rev.*, 39:1203–1217.

Lim, E. J., Ober, T. J., Edd, J. F., Desai, S. P., Neal, D., Bong, K. W., Doyle, P. S., McKinley, G. H., and Toner, M. (2014). Inertio-elastic focusing of bioparticles in microchannels at high throughput. *Phys. Rev. X*, 5.

Maria, M. S., Kumar, B. S., Chandra, T. S., and Sen, A. K. (2015). Development of a microfluidic device for cell concentration and blood cell-plasma separation. *Biomedical Microdevices*, 17(6):115.

Masaeli, M., Sollier, E., Amini, H., Mao, W., Camacho, K., Doshi, N., Mitragotri, S., Alexeev, A., and Di Carlo, D. (2012). Continuous inertial focusing and separation of particles by shape. *Phys. Rev. X*, 2:031017.

Maxey, M. R. and Riley, J. J. (1983). Equation of motion for a small rigid sphere in a nonuniform flow. *The Physics of Fluids*, 26(4):883–889.

Mossige, E. J., Jensen, A., and Mielnik, M. M. (2016). An experimental characterization of a tunable separation device. *Microfluidics and Nanofluidics*, 20(12):160.

Nam, J., Shin, Y., Tan, J. K. S., Lim, Y. B., Lim, C. T., and Kim, S. (2016). High-throughput malaria parasite separation using a viscoelastic fluid for ultrasensitive pcr detection. *Lab Chip*, 16:2086–2092.

Warkiani, M. E., Tay, A. K. P., Khoo, B. L., Xiaofeng, X., Han, J., and Lim, C. T. (2015). Malaria detection using inertial microfluidics. *Lab Chip*, 15:1101–1109.

Yamada, M. and Seki, M. (2005). Hydrodynamic filtration for on-chip particle concentration and classification utilizing microfluidics. *Lab Chip*, 5:1233–1239.

Yamada, M., Seko, W., Yanai, T., Ninomiya, K., and Seki, M. (2017). Slanted, asymmetric microfluidic lattices as size-selective sieves for continuous particle/cell sorting. *Lab Chip*, 17:304–314.